Contents lists available at ScienceDirect

Applied Catalysis B: Environmental

Deactivation mechanism of Ni supported on Mg-Al spinel during autothermal reforming of model biogas

Mathilde Luneau, Elia Gianotti, Frédéric C. Meunier, Claude Mirodatos, Eric Puzenat, Yves Schuurman, Nolven Guilhaume*

Université de Lyon, Institut de Recherches sur la Catalyse et l'Environnement de Lyon, IRCELYON UMR5256 CNRS, 2 Avenue Albert Einstein, F-69626 Villeurbanne Cedex, France
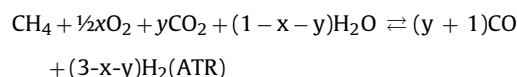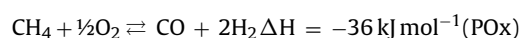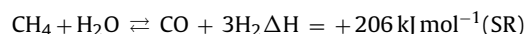
A B S T R A C T

Nickel supported on Mg-Al oxides was studied in the autothermal reforming (ATR) of model biogas at 700 °C. $Ni/Mg_{0.4}Al_2O_{3.4}$ deactivated with time on stream and the cause of deactivation was investigated and identified. Ni was readily oxidized to NiO in the presence of O_2. While NiO was essentially inactive for the reforming reaction, this oxide was yet active for methane combustion. Exhaustion of the O_2 supply at front of the catalyst bed enabled the remaining CH_4 to be steam and dry reformed on the metallic Ni left downstream. Gradual formation of $NiAl_2O_4$ spinel was also observed, likely caused by the higher temperature prevailing in the exothermic combustion zone that favors the diffusion of nickel cations into the alumina structure. In contrast to NiO, $NiAl_2O_4$ spinel was poorly active for CH_4 oxidation. The frontline associated with the formation of the $NiAl_2O_4$ spinel phase eventually reached the end of the catalyst bed, resulting in a complete loss of activity. No significant coke deposition could be evidenced here. The Ni deactivation profile was adequately fitted using a methane ATR kinetic model that included a linear decrease in the number of Ni metallic sites. Addition of $Rh/Mg_{1.1}Al_2O_{4.1}$ in front of a nickel-based catalyst led to a stable activity. Using this dual-bed system, no $NiAl_2O_4$ formation was identified after reaction.

© 2016 Elsevier B.V. All rights reserved.

1. Introduction

Biogas is a gas mixture primarily composed of methane and carbon dioxide produced by anaerobic digestion of biomass. Biogas can be reformed into hydrogen-rich syngas for fuel-cell applications. The reforming reactions include steam reforming (SR), dry reforming (DR), partial oxidation (POx) and autothermal reforming (ATR).

$$CH_4 + H_2O \rightleftarrows CO + 3H_2 \quad \Delta H = +206\,kJ\,mol^{-1} (SR)$$

$$CH_4 + CO_2 \rightleftarrows 2CO + 2H_2 \quad \Delta H = +247\,kJ\,mol^{-1} (DR)$$

$$CH_4 + \tfrac{1}{2}O_2 \rightleftarrows CO + 2H_2 \quad \Delta H = -36\,kJ\,mol^{-1} (POx)$$

$$CH_4 + \tfrac{1}{2}xO_2 + yCO_2 + (1 - x - y)H_2O \rightleftarrows (y + 1)CO$$
$$+ (3\text{-}x\text{-}y)H_2 (ATR)$$

ATR reactions include the exothermic oxidation of methane with O_2, which provides the energy needed for the endothermic reforming reactions.

Catalytic reforming of methane is traditionally performed over Ni-based catalysts, since those provide acceptable activity and are inexpensive metals. Noble metals such as Rh, Ru, Pd and Pt are also active and less prone to deactivation, but the metal price is usually prohibitive [1,2].

In the literature, deactivation during methane or biogas reforming reactions over Ni-based catalysts is usually related to poisoning or carbon deposition [3,4]. The most studied poisons are H_2S and other sulfur-containing compounds [4].

Carbon formation has been observed in many studies. Different types of carbon can lead to deactivation. Encapsulating carbon forms a graphite layer covering the nickel particles that leads to the loss of active metal surface. Whisker-like carbon formation does not entail immediate deactivation of the Ni-surface, but leads to a blockage of the porosity and catalyst breakdown, whereas extensive whiskers growth can also plug the reactor [4,5].

Loss of active metal surface by sintering is another cause of deactivation of nickel catalysts during reforming reactions [6,7]. It is favored by high temperatures and high pressures of steam [5].

During SR and POx reaction, Ni has been reported to react with alumina to form inactive $NiAl_2O_4$ [4,8,9]. Ni^{2+} ions can diffuse into the cationic vacancies present in γ-Al_2O_3, resulting in the formation of nickel aluminate. The temperature at which nickel aluminate starts forming is not well defined.

While deactivation during SR, DR or POx over Ni-based catalyst has been extensively investigated over the years, few deactivation studies have been reported on ATR of methane and even less on ATR of biogas. Araki et al. performed ATR of biogas on a Ni/Mg/Al catalyst and assigned the observed deactivation to the oxidation of metallic Ni into Ni_2O_3 [10]. Similarly, Nagaoka et al. observed that a Ni/MgAlO$_x$ catalyst derived from hydrotalcite structure deactivated slowly during ATR of methane, and the catalyst deactivation was related to the formation of oxidized Ni species that were not clearly identified [11].

Long-term stability is seldom assessed and when deactivation is observed, it is rarely unambiguously and quantitatively addressed. Hypotheses on the loss of activity during ATR of methane and biogas can vary from nickel oxidation [6,12,13] to phase transformation or active metal sintering [14]. Moreover, even though carbon deposition is less likely to occur because of the presence of molecular oxygen [10], it has also been speculated to be the cause of deactivation in some cases [15,16].

In the present work, ATR of model biogas over Ni catalysts supported on Mg-Al-O spinel oxides was performed at 700 °C with conditions $H_2O/CH_4 = 3$, $O_2/CH_4 = 0.5$ and $CH_4:CO_2 = 60\%:40\%$. In terms of activity, there is an agreement on the fact that Ni/Mg-Al mixed oxides catalysts are more active than Ni/γ-Al_2O_3 and Ni/α-Al_2O_3 [6]. As discussed before, Ni catalyst deactivation can originate from different phenomena. Poisoning by sulfur is not relevant in our case because our study will focus on S-free model-biogas. Combining O_2/CH_4 ratio of 0.5 and high steam pressure should not favor carbon formation. Moreover, $MgAl_2O_4$ is expected to limit the formation of inactive $NiAl_2O_4$, since the cationic sites of γ-Al_2O_3 into which Ni^{2+} ions could diffuse are already occupied by Mg^{2+} ions [17]. The long-term deactivation behavior with time-on-stream was studied on a Ni catalyst supported on $Mg_xAl_2O_{3+x}$. This study is, to our knowledge, the first that precisely and quantitatively describes the complex cascade of events leading to full deactivation of Ni-based catalysts during ATR of biogas. The Ni species formed with time-on-stream during the deactivation process were identified and quantified using UV–vis spectroscopy. A kinetic model including a linear decrease in the number of Ni metallic sites fitted adequately the experimental deactivation profiles and allowed to calculate the Ni deactivation rate. Once the deactivation process understood, a strategy to ensure high activity and stability using the lowest possible noble metal content is proposed.

2. Materials and methods

2.1. Catalyst preparation

2.1.1. MgAl$_2$O$_4$ preparation with different Mg:Al ratios
Magnesium spinel supports were prepared by co-precipitation following a procedure described elsewhere [18]. An aqueous solution containing Mg and Al nitrates (Sigma-Aldrich and Fluka) was gradually added to an aqueous solution of ammonium carbonate (Sigma Aldrich) under fast stirring. Three similar preparations were carried out with three different Mg:Al ratios. The precipitates were aged for 3 h at 60 °C and pH 9. After centrifugation and several washing cycles at room temperature, the powders were dried overnight at 100 °C. The powders were then calcined at 800 °C

for 5 h in air in order to obtain $Mg_{0.4}Al_2O_{3.4}$, $Mg_{0.7}Al_2O_{3.7}$ and $Mg_{1.1}Al_2O_{4.1}$.

2.1.2. Impregnation of Ni and Rh
Ni was deposited on the three different spinel supports by deposition-precipitation using nickel nitrate $Ni(NO_3)_2 \cdot 6H_2O$ (Fluka) and urea (Sigma-Aldrich). Stirring was continued for 4 h while the temperature was increased to 100 °C in order to remove excess urea. After centrifugation and several washings with de-ionized water, the samples were dried at 100 °C overnight and calcined at 550 °C for 4 h in air in order to obtain 5 wt.% $Ni/Mg_{0.4}Al_2O_{3.4}$ (NM0.4), 5 wt.% $Ni/Mg_{0.7}Al_2O_{3.7}$ (NM0.7), and 5 wt.% $Ni/Mg_{1.1}Al_2O_{4.1}$ (NM1.1).

0.05 wt.% $Rh/Mg_{1.1}Al_2O_{4.1}$ (RM1.1) was also prepared by wet impregnation of $Mg_{1.1}Al_2O_{4.1}$ with a solution containing rhodium nitrate $Rh(NO_3)_3 \cdot 2H_2O$ (Alfa Aesar). The solution was stirred for 4 h. After evaporation of water, the slurry was dried at 120 °C overnight and calcined at 550 °C for 4 h in air. The Rh composition was confirmed by chemical analysis (0.0524 wt.%).

2.1.3. NiAl$_2$O$_4$ preparation
$NiAl_2O_4$ (NA) spinel was prepared by co-precipitation. An aqueous solution of ammonium hydroxide NH_4OH (concentration of 0.6 M) was added drop by drop into an aqueous solution containing Ni and Al nitrates (Fluka) with a Al:Ni molar ratio of 2:1 (concentrations of 0.17 and 0.34 mol L^{-1} respectively). During addition, the solution was continuously stirred and the evolution of pH was followed closely. The addition of NH_4OH was stopped at pH 8.5. After centrifugation and several washing cycles at room temperature, the powder was dried overnight at 100 °C, then calcined at 800 °C for 5 h in air.

2.2. Catalyst characterization

Powder X-ray diffraction patterns (XRD) were recorded on a Bruker D5005 diffractometer using the CuK radiation at $\lambda = 1.5418$ Å.

Chemical analysis of the fresh catalysts was performed by inductively coupled plasma atomic emission spectroscopy (ICP-AES) using a Jobin Yvon Activa Spectrometer D ICP-OES in order to determine the Ni loadings and the Ni:Al and Mg:Al molar ratios.

Transmission Electron Microscopy (TEM) examinations were performed on a JEOL 2010 microscope operating at 200 kV. Specific surface areas were measured by nitrogen adsorption at −196 °C with a BELSORP-Mini (Bel-Japan) instrument. XPS analyses were carried out with an AXIS Ultra DLT (Kratos Analyticals) spectrometer.

UV–vis diffuse reflectance spectroscopy (UV–vis-DRS) was performed on the samples in order to investigate the nature of the nickel species present before and after reaction. A Deuterium-Halogen lamp emitting between 210 and 1000 nm was used as the light source. The light was conducted to an optical fiber probe (FCR-7UV-400-2ME). Reflectance was measured by a Charge Couple Device (CCD) detector equipped with a monochromator in a Czerny-Turner configuration. The samples were mixed with BaSO$_4$, which was also used as "white" reference material. For all spectra, the simplified Kubelka-Munk function is represented. The dilution of samples with BaSO$_4$ was sufficient to consider that light scattering constant was similar for all measurement.

2.3. Catalytic tests and deactivation study

ATR tests were performed at atmospheric pressure using a quartz fixed bed reactor (i.d. = 4 mm). The catalysts were sieved beforehand to obtain particle sizes between 100 and 200 μm. The catalyst mass used varied from 20 to 40 mg. The bed height and thus

Table 1
Reaction conditions for the ATR of model biogas.

Temperature (°C)	700
Pressure	1.1–1.3 bar
Steam/CH_4	3
O_2/CH_4	0.5
CH_4:CO_2 (vol.%:vol.%)	60:40

the GHSV varied depending on the catalyst mass used for reaction. In-situ pre-reduction of the catalysts was carried out for 3.5 h at 800 °C in a mixture of H_2-Ar (4:1; vol:vol). ATR was performed at 700 °C with a 42% steam, 14% CH_4, 9% CO_2, 7% O_2 and 28% Ar reactant mixture. This composition corresponded to the reaction of model biogas (CH_4:CO_2 = 60%:40% vol:vol) with O_2 and steam in accordance with ratios O_2/CH_4 = 0.5 and Steam/CH_4 = 3 (Table 1). The Ar concentration in the inlet stream corresponded to the amount of N_2 that would be present if oxygen were supplied as air. Online analysis of the effluent gases was performed with a mass spectrometer (MS) using the Ar signal as internal standard for quantification. The ion current intensities were converted to molar flows knowing the molar flow rate of Ar and the sensitivity coefficient of each m/z fragment relative to Ar, which was constant. The MS response was calibrated using different partial pressures of all relevant compounds diluted in argon. The liquid water flow rate was precisely controlled by a calibrated HPLC pump (Shimadzu LC-20AD) and dispensed in an evaporator kept at 200 °C. The use of Ar as internal standard allowed compensating for the gas expansion resulting from the reaction.

Equilibrium conversions and compositions were calculated using the HSC-Chemistry software (version 6.0). These thermodynamic calculations are based on the minimization of the Gibbs free energy.

3. Results

3.1. Characterization of fresh catalysts

The nickel loadings are reported in Table 2. The amount of deposited Ni was close to the nominal value of 5 wt.% for NM0.4, NM0.7 and NM1.1. NA presented a Ni composition of 31.3 wt.% corresponding to a Ni:Al ratio of 0.49, close to that expected for the $NiAl_2O_4$ spinel. Mg:Al ratios were calculated from ICP analyses of the supports before nickel impregnation.

The NA structure was investigated by XRD after calcination at 800 °C (Fig. 1). It exhibited only the characteristic lines of the $NiAl_2O_4$ spinel phase. Neither Ni nor NiO were observed. XRD analysis of the fresh Ni/$MgAlO_x$ catalysts after Ni impregnation was performed after calcination in air at 550 °C. NM0.4 and NM0.7 presented similar diffractograms. Typical lines for $MgAl_2O_4$ spinel were evidenced while neither Ni nor NiO lines were observed. The metal loading (5 wt.%) could be too low to observe specific lines from NiO. The particles might also be too small or, given that $MgAl_2O_4$ and $NiAl_2O_4$ structures are very similar, nickel particles might also interact strongly with the support. In addition to the spinel phase, NM1.1 and RM1.1 clearly displayed the weak but characteristic lines of a crystalline phase consistent with the pattern of MgO. In the case of NM1.1, these lines could also correspond to NiO.

TEM examination of NM0.7 catalyst, previously reduced under H_2 at 700 °C, revealed that Ni was homogeneously dispersed on the support (Fig. 2). The Ni particle size was essentially in the 2.5–4.5 nm range, with some larger particles around 6–7 nm. The contrast between the Ni and the spinel support was poor, probably due to nickel oxidation into NiO in air during sample preparation for microscopy studies.
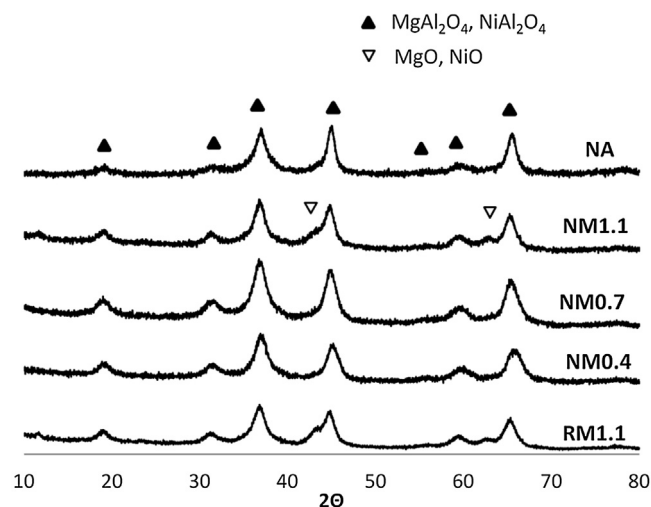

Fig. 1. X-ray diffractograms of NA after calcination at 800 °C and fresh catalysts NM0.4, NM0.7, NM1.1, RM1.1 after calcination in air at 550 °C.
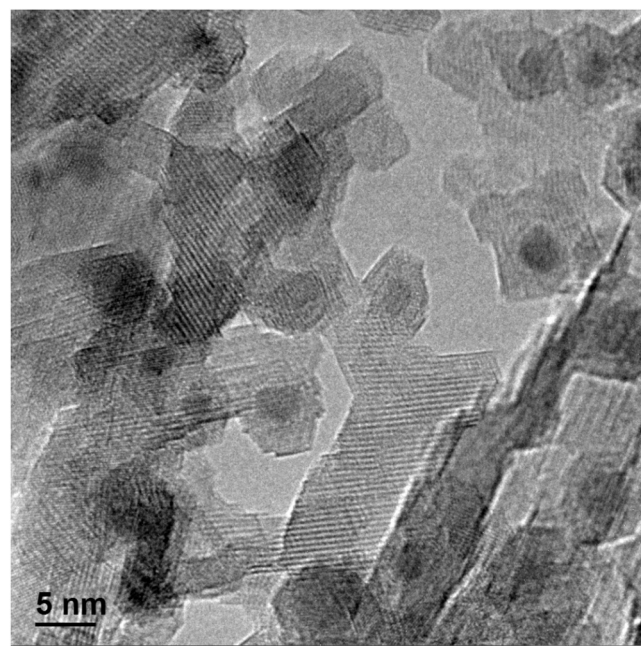

Fig. 2. TEM micrograph of fresh NM0.7 catalyst.

3.2. Autothermal reforming of model biogas

3.2.1. Evaluation of the temperature profile along the catalytic bed during ATR of model biogas over NM0.4

ATR of model biogas was performed over 20 mg of NM0.4 at 700 °C (GHSV = 40 000 h^{-1}). Full CH_4 and O_2 conversions were observed from the beginning of the reaction (Fig. 3a). This corresponds to equilibrium conversions at this temperature. Hydrogen and carbon monoxide production was stable (Fig. 3b) with a H_2/CO molar ratio equal to 2.5. After 6.7 h, CH_4 and O_2 conversions decreased sharply. H_2 and CO productions dropped similarly until complete deactivation of the catalyst. NM0.4 was fully inactive after 7 h.

The catalyst was black after reduction and light blue/green after complete deactivation. Another important observation was that when the reaction was stopped before complete deactivation, the catalyst bed exhibited two regions with different colors: light blue/green at the reactor inlet and black at the outlet.

Table 2
Chemical compositions of prepared catalysts from ICP analyses and BET specific surface areas.

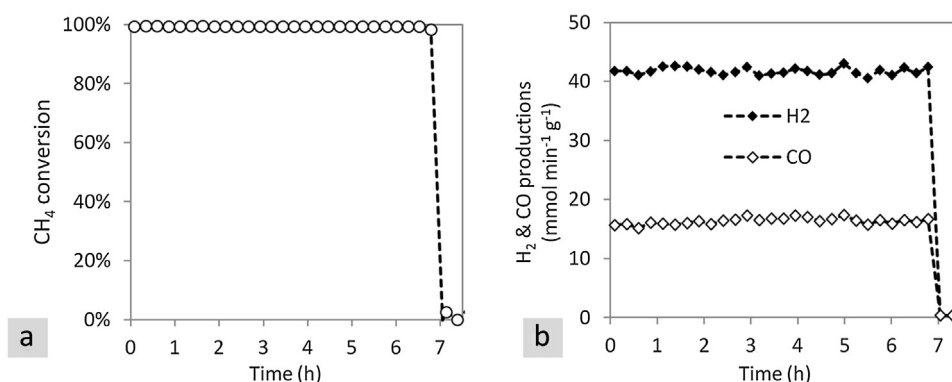|	Code	Ni loading (wt.%)	Mg:Al molar ratio	Ni:Al molar ratio	Surface area ($m^2 \, g^{-1}$)
5 wt.% Ni/Mg$_{0.4}$Al$_2$O$_{3.4}$	NM0.4	5.0	0.21	–	152
5 wt.% Ni/Mg$_{0.7}$Al$_2$O$_{3.7}$	NM0.7	4.8	0.34	–	158
5 wt.% Ni/Mg$_{1.1}$Al$_2$O$_{4.1}$	NM1.1	5.1	0.55	–	189
NiAl$_2$O$_4$	NA	31.3	–	0.49	94
0.05 wt.% Rh/Mg$_{1.1}$Al$_2$O$_{4.1}$	RM1.1	–	0.55	–	n.a.

n.a.: not analyzed.

Fig. 3. a) CH_4 conversion and b) H_2 and CO productions (mmol min^{-1} g^{-1}) during ATR of model biogas on 20 mg of NM0.4. Reaction conditions: T = 700 °C, Steam/CH$_4$ = 3, O$_2$/CH$_4$ = 0.5, CO$_2$:CH$_4$ = 40:60, GHSV = 40 000 h^{-1}.
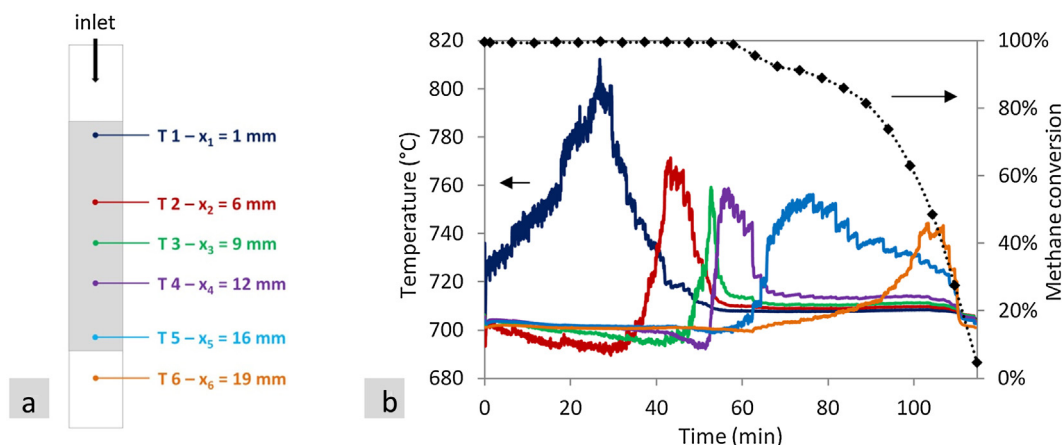

Fig. 4. a) schematic representation of the reactor with the positions of the six thermocouples. b) Evolution of the temperature (left axis) and methane conversion (right axis) over time during ATR reaction on 20 mg of NM0.4 at 700 °C, Steam/CH$_4$ = 3, O$_2$/CH$_4$ = 0.5, CO$_2$:CH$_4$ = 40:60, GHSV = 40 000 h^{-1}.

The experiment was repeated with six thin thermocouples (o.d. 0.5 mm) placed into the catalytic bed at six different locations. The total catalytic bed height was about 17 mm (i.d = 4 mm). The thermocouples T1–T6 were placed at x = 1, 6, 9, 12, 16, 19 mm, respectively (Fig. 4a).

The temperature was recorded every 3 s (Fig. 4b). It should be noted that a blank experiment performed under identical conditions in the reactor containing only the thermocouples and quartz wool but no catalyst showed that neither methane nor oxygen conversion took place on the thermocouples. Therefore, the observed activity resulted only from the catalyst.

From the start of the reaction until 26.8 min, the temperature T1 measured by the first thermocouple increased steadily until reaching a maximum of 812 °C. Meanwhile, T2 decreased slightly from 700 °C to 695 °C. The temperatures measured by the 4 other thermocouples located downstream remained constant, revolving around 700 °C. After reaching its maximum, T1 dropped while T2 increased to reach a maximum of 771 °C after 43.3 min, while T3

slightly declined and T4–T6 stayed stable. The same phenomena were observed for each thermocouple until complete deactivation of the catalyst. These observations can be rationalized by proposing that an exothermal combustion zone progressed along the catalyst bed during reaction until complete deactivation. Complete deactivation occurred after 115 min, which was much shorter than the deactivation time observed during the first test (Fig. 3) even though both tests were performed under identical conditions. This discrepancy probably resulted from preferential pathways created when introducing the six thermocouples into the catalytic bed, which allowed unconverted oxygen to rapidly oxidize the metallic Ni present in these preferential pathways and consequently increased the deactivation rate. After the end of the reaction, the temperatures all returned to their initial values, around 700 °C.

3.2.2. ATR of biogas over pure NiAl$_2$O$_4$ and NiO

The reaction was carried out over 40 mg of NiAl$_2$O$_4$ at a GHSV = 80 000 h^{-1}. No pre-treatment step was performed before
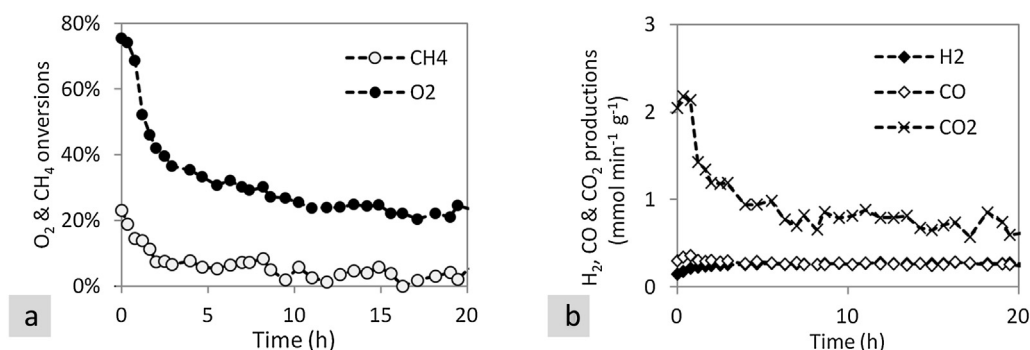
Fig. 5. a) O_2 and CH_4 conversions and b) H_2, CO and CO_2 productions (mmol min^{-1} g^{-1}) during ATR of model biogas over 40 mg of NiAl$_2$O$_4$ at 700 °C, Steam/CH$_4$ = 3, O_2/CH$_4$ = 0.5, CO_2:CH$_4$ = 40:60, GHSV 80 000 h^{-1}.
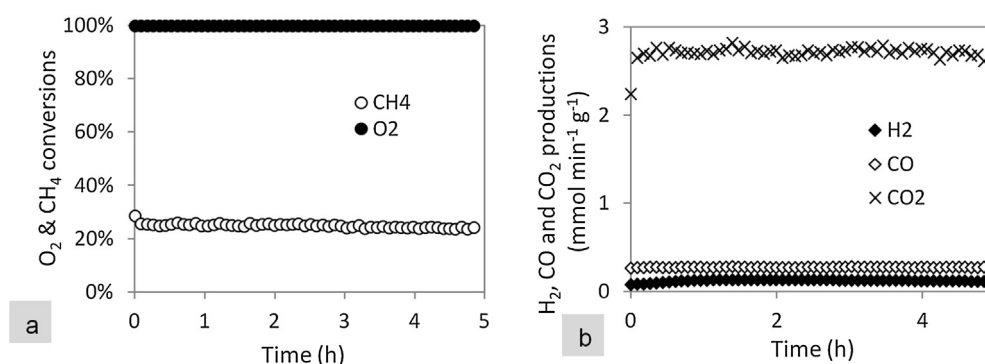
Fig. 6. a) CH_4 and O_2 conversions and b) H_2, CO and CO_2 productions (mmol min^{-1} g^{-1}) during ATR of model biogas over 40 mg of NiO at 700 °C, Steam/CH$_4$ = 3, O_2/CH$_4$ = 0.5, CO_2:CH$_4$ = 40:60, GHSV 80 000 h^{-1}.

reaction so as to maintain nickel oxidized into the spinel structure. O_2 and CH_4 conversions as well as production of CO_2, H_2 and CO (μmol min^{-1}) are shown in Fig. 5.

O_2 and CH_4 conversions started from 75 and 23%, respectively, and lead to the production of slightly more than 2 mmol min^{-1} g^{-1} of CO_2. The conversions decreased steadily during 8 h, after which a stable production of ca. 0.8 mmol min^{-1} g^{-1} CO_2 due to conversions of about 20–25% of O_2 and 3–6% of CH_4. During the 20 h of reaction, almost no production of H_2 and CO was observed (<0.3 mmol min^{-1} g^{-1}). This shows that NiAl$_2$O$_4$ is poorly active for methane total oxidation and even less active for the reforming of methane.

The same reaction was carried out on pure NiO. Full O_2 conversion and 25% CH_4 conversions were observed, corresponding to the combustion of methane into CO_2 allowed by the oxygen present in the feed, since the conversion of oxygen was total (Fig. 6). This shows that NiO is active for methane oxidation but not for steam or CO_2 reforming.
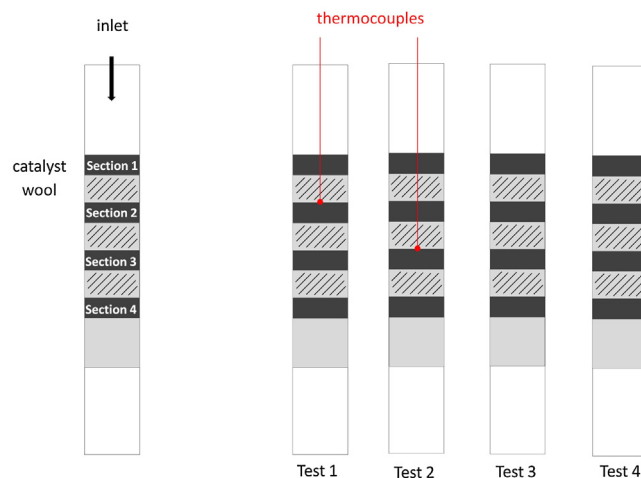
3.2.3. ATR of model biogas on NM0.4 using a reactor divided into 4 beds

Four ATR reactions were performed in 4 identical reactors prepared with NM0.4. Each of them was divided into 4 layers of 10 mg catalyst, each separated with quartz wool. Fig. 7 depicts the schematic of experiments.

In the first test, a thermocouple was placed on top of the second catalyst layer. In the second test, it was placed on top of the third catalyst layer. Reactions 1 and 2 were stopped when the temperatures measured by the thermocouples reached a maximum. Methane conversions were still complete at these points. The third test was stopped when the methane conversion reached 96%. The fourth test was stopped after complete deactivation.

Fig. 7. Schematic of experiments for the ATR tests on NM0.4.

Fig. 8 displays photographs of the reactors before reaction and after each test. A first observation is that the catalyst layers are either black or light blue/green. After test 1, most layers exhibit a black color except the top of the first layer, which is light blue, whereas the four layers display a light blue color after complete deactivation (test 4).

The catalyst layers were analyzed separately by UV–vis-DRS in order to study the coordination states of the nickel species. This technique seemed well suited since the Ni, NiO and NiAl$_2$O$_4$ compounds display distinct colors (black, green and blue, respectively). The relative reflectance was calculated by using BaSO$_4$ as white reference.
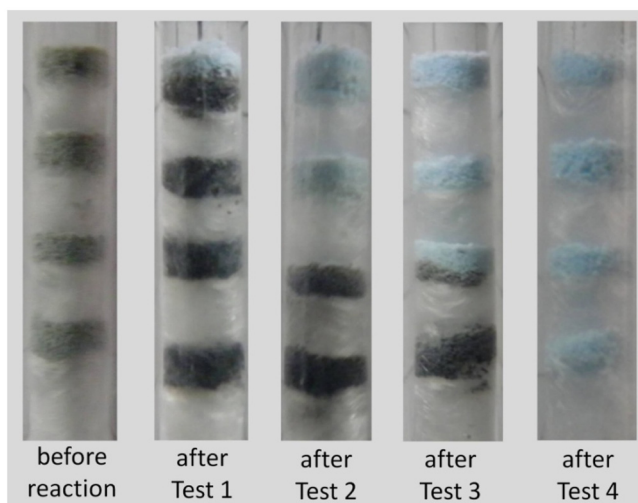
Fig. 8. Photographs of the catalysts after tests 1–4 on NM0.4 (m = 4 × 10 mg). Reaction conditions: T = 700 °C, Steam/CH$_4$ = 3, O$_2$/CH$_4$ = 0.5, CO$_2$:CH$_4$ = 40:60, GHSV = 66 700 h^{-1}. (For interpretation of the references to color in the text, the reader is referred to the web version of this article.)
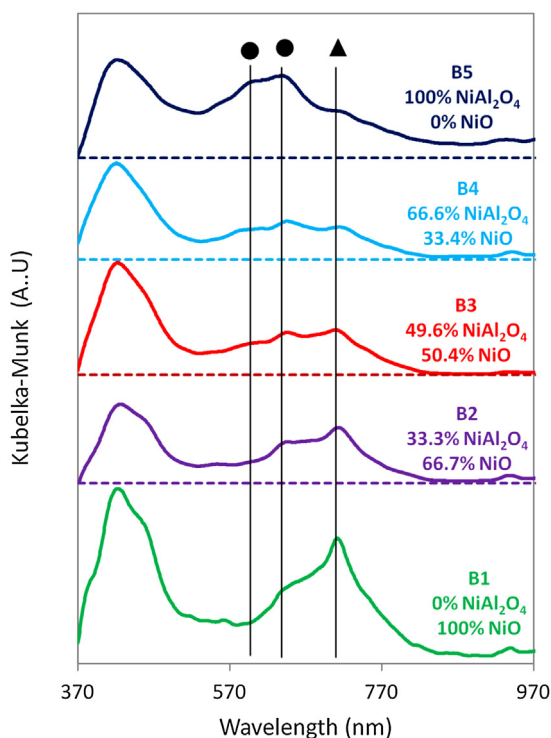

Fig. 9. Kubelka-Munk Spectra of benchmarcks presenting (●) tetrahedrally coordinated Ni^{2+} in NiAl$_2$O$_4$ at 600 and 640 nm and (▲) octahedrally coordinated Ni^{2+} in NiO at 715 nm.

A calibration curve was drawn using five samples as benchmarks. The benchmarks were prepared by mixing known proportions of pure NiO and NiAl$_2$O$_4$. Each mixture was then diluted with Mg$_{0.4}$Al$_2$O$_{3.4}$ in order to emulate the catalyst used for the reaction. The total amount of nickel to be added was thus calculated in order to correspond to a 5 wt.% Ni catalyst. The benchmarks were analyzed by UV–vis-DRS. Fig. 9 shows the five spectra.

The spectra were offset for the sake of clarity. It should be noted that the pure support Mg$_{0.4}$Al$_2$O$_{3.4}$ is white. It was also analyzed and showed no absorption in the 370–970 nm region (not shown). B1 composed of 100% NiO − 0% NiAl$_2$O$_4$ displayed one absorp-

Table 3
XPS analysis of surface carbon for NM0.7 catalyst.

	Surface carbon (at.%)
NM0.7 reduced ex-situ, contact with air	8.8
NM0.7 reduced in-situ, no contact with air	0.9
NM0.7 deactivated catalyst	4.0

tion band at 715 nm. B5 composed of 100% NiAl$_2$O$_4$ displayed two important absorption bands at 600 nm and 640 nm. The absorption bands at 600 and 640 nm were attributed to Ni^{2+} ions in tetrahedral coordination in NiAl$_2$O$_4$ [19,20]. The band located at 715 nm is typical of Ni^{2+} ions octahedrally coordinated in NiO. The four catalyst sections were then analyzed (Fig. 10).

The ratio of the absorptions Abs (715 nm)/Abs (600 nm) was used to determine the proportion of nickel spinel and nickel oxide phases in the non-dark zones, which were obscured by the presence of strongly absorbing metallic Ni. Only the spinel phase could be observed, the proportion of NiO being always negligible, except for the section 1 of test 1 and section 2 of test 2, for which it accounted for about 5 wt.%.

3.2.4. ATR of model biogas on nickel catalysts supported on different Mg$_x$Al$_2$O$_{3+x}$ supports

NM0.4, NM 0.7 and NM 1.1 were tested for the ATR reaction under similar conditions. The reactions were started under standard conditions (steam/CH$_4$ = 3, O$_2$/CH$_4$ = 0.5, CH$_4$:CO$_2$ = 60:40) at a GHSV of 40 000 h^{-1}. During the first 2 h all catalysts presented full conversions of both CH$_4$ and O$_2$. Those also presented the same performances in terms of selectivity and production of H$_2$, CO and CO$_2$ (Fig. 11). The GHSV was then increased, to accelerate ageing.

After 2 h, the GHSV was increased to 60 000 h^{-1}. NM0.4 deactivated immediately (Fig. 12). NM0.7 deactivated 45 min later, after 2.75 h of reaction. However NM1.1 still exhibited full conversions of methane and oxygen. The GHSV was increased to 100 000 h^{-1} after a short step at 80 000 h^{-1}. After 20 h, this catalyst still exhibited 95% methane conversion and complete oxygen conversion.

After reaction, NM0.4 (deactivated), NM0.7 (also deactivated) and NM1.1 (still active) were analyzed by UV–vis-DRS (Fig. 13). The ratio of absorptions Abs (715 nm)/Abs (600 nm) was calculated. NM0.4 and NM0.7 were composed of 97% and 98% of NiAl$_2$O$_4$ after deactivation. Although NM1.1 was still active when the reaction was stopped, some spinel phase was observed at the front of the catalyst bed. The non-metallic nickel phase was composed of 79% NiAl$_2$O$_4$–21% NiO.

In order to assess the possible role of carbon deposition in the deactivation process, a TPO was performed on the deactivated NM0.7 catalyst, directly after reaction and analyzing the CO$_2$ mass with the online mass spectrometer. The amount of CO$_2$ was undetectable, possibly because the catalyst mass was low (20 mg). XPS analyses were also performed on the fresh catalyst after ex-situ reduction, in-situ reduction in the XPS preparation cell and on the spent catalyst. The results are presented in Table 3.

The fresh NM0.7 catalyst, previously calcined in air and reduced ex-situ, contained about 9 at.% of surface carbon. Since the catalysts were prepared from inorganic precursors in the absence of any organic solvent, this carbon probably originated from surface carbonates formed by contact with air on the basic Mg$_{0.7}$Al$_2$O$_{3.7}$ support. C1s spectra (not shown) displayed a peak at 289 eV, which can be attributed to carbonates. In situ reduction at 700 °C performed in the preparation chamber of the XP spectrometer immediately before analysis showed that this treatment eliminated a large fraction of these carbonates, probably by simple thermal decomposition. The spent NM0.7 catalyst (deactivated) contained actually less surface carbon than the fresh catalyst, showing clearly that carbon deposition is not involved in the deactivation process.
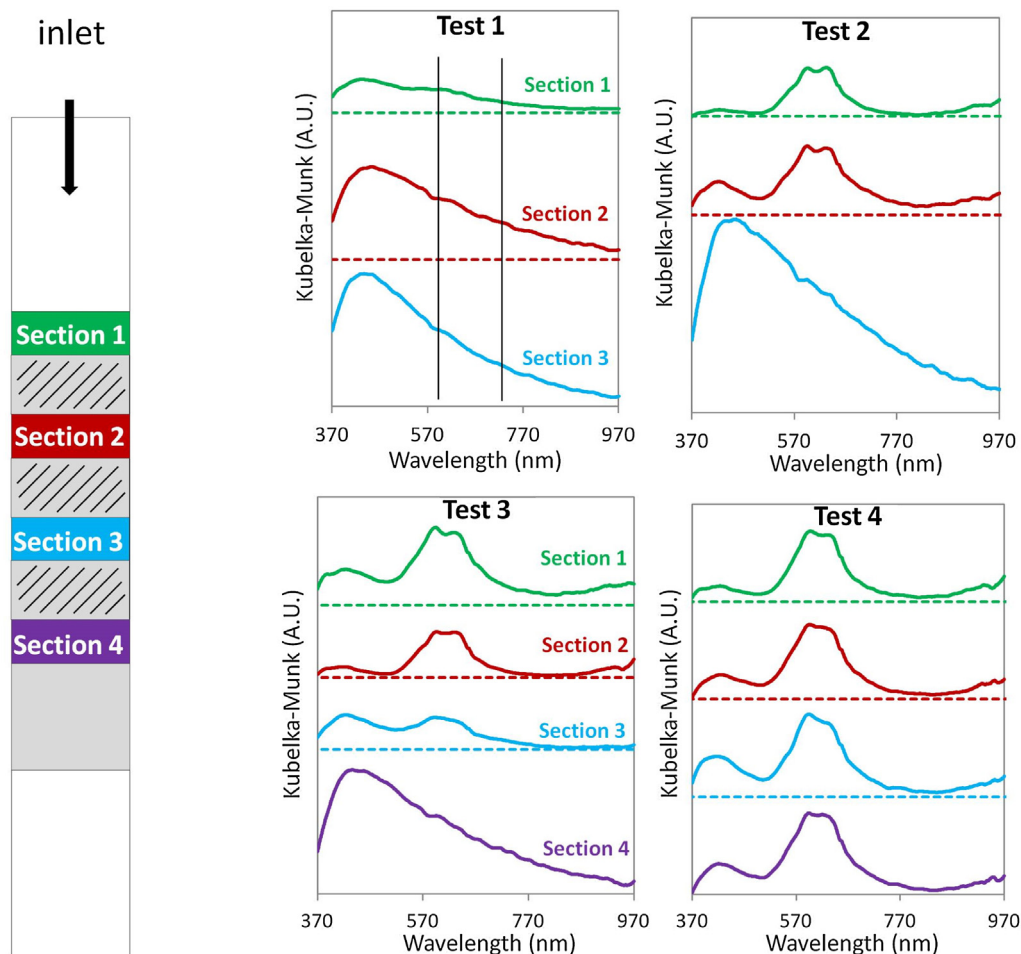
Fig. 10. Kubelka-Munk spectra of reactor sections after catalytic tests 1–4 on NM0.4 (samples presented in Fig. 8).
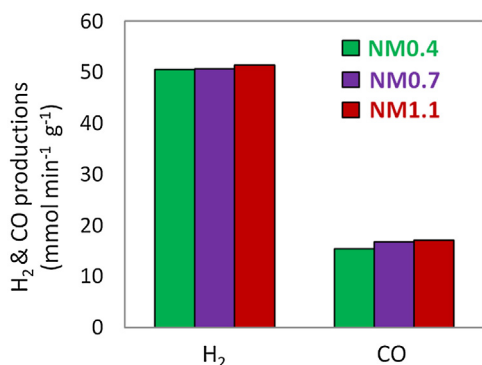

Fig. 11. H_2 and CO productions during the first two hours of ATR of model biogas over 20 mg of NM0.4, NM0.7 and NM1.1. Reaction conditions T = 700 °C, Steam/CH_4 = 3, O_2/CH_4 = 0.5, CO_2:CH_4 = 40:60, GHSV = 40 000 h^{-1}.

From these results, it can be concluded that the catalyst resistance to deactivation is highly dependent on the composition of the support and more specifically to the Mg:Al ratio.

3.2.5. Activity of Rh sample and dual bed

A dual-catalyst bed system was implemented. A Rh catalyst supported on $Mg_{1.1}Al_2O_{4.1}$ (RM1.1) was chosen as the first catalyst bed in order to perform the combustion of methane. Rhodium is a very stable methane oxidation catalyst because metallic Rh is the thermodynamically stable phase at high temperature, even in the presence of oxygen. The second catalyst bed consisted of NM0.4 to catalyze the reforming reactions, with no O_2 left to form an inactive $NiAl_2O_4$ spinel phase. Such a dual catalyst design has already been reported in the literature for the POx of methane [21–23].

RM1.1 was first tested alone. The reaction was started on 20 mg at a GHSV of 40 000 h^{-1} then increased step by step to 100 000 h^{-1} following the same procedure as on the nickel catalysts. Fig. 14 shows O_2 and CH_4 conversions as well as H_2 and CO productions.

At any time and GHSV, the oxygen conversion was always complete. During the first two hours at GHSV = 40 000 h^{-1}, CH_4 conversion decreased from 80% until reaching a stable conversion of 64%. The catalyst then showed very high stability for 20 h even at high GHSV. It showed incomplete CH_4 conversion ranging from 64 to 71% depending on the GHSV.

A dual-bed catalyst was prepared with 8 mg of RM1.1 placed on top of two layers (10 mg each) of NM0.4 (Fig. 15).

Fig. 16 shows the performances in terms of CH_4 conversion and H_2 and CO productions. The performances in terms of H_2/CO selectivity and CO_2 production were similar to those of NM0.4 alone (Fig. 3). Indeed, H_2/CO molar ratio was equal to 2.5. While NM0.4 used alone fully deactivated after only 7 h of reaction, the dual bed catalyst showed full CH_4 and O_2 conversion for more than 20 h.

The reaction was stopped in order to investigate the presence of $NiAl_2O_4$. Both sections of nickel-based catalyst were black and did not display any traces of blue spinel (Fig. 17a). UV–vis-DRS analyses carried out on the two sections confirmed these observations (Fig. 17b): the spectra of these two sections were similar to some sections presented in Fig. 9 when the catalyst contained only metallic nickel.
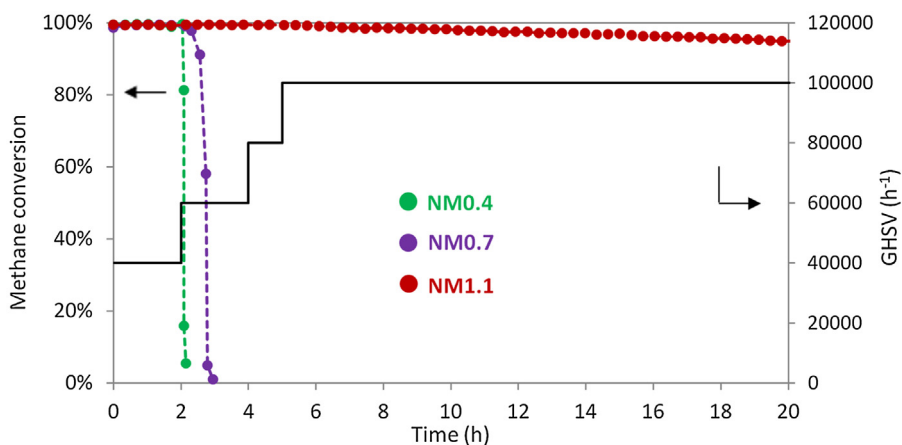
Fig. 12. Methane conversion during ATR reaction on 20 mg NM0.4, NM0.7 and NM1.1. Reaction conditions: T = 700 °C, Steam/CH$_4$ = 3, O$_2$/CH$_4$ = 0.5, CO$_2$:CH$_4$ = 40:60, GHSV ranging from 40 000 to 100 000 h^{-1}.
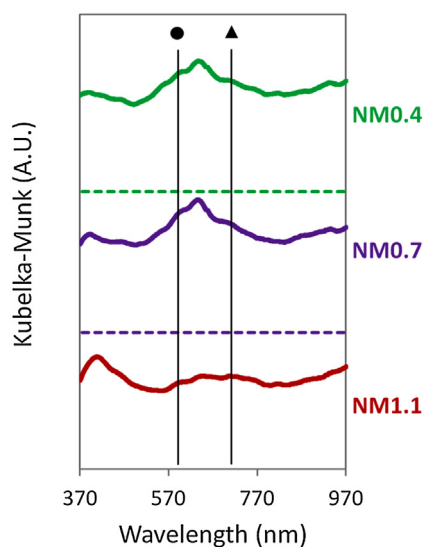
Fig. 13. Kubelka-Munk spectra of NM0.4 (deactivated), NM0.7 (deactivated) and NM1.1 (still active).

Fig. 15. Scheme of the reactor prepared with 8 mg RM1.1 on top of two layers of 10 mg of NM0.4 each.

4. Discussion

Deactivation of Ni-based catalysts during methane or biogas reforming is usually reported to be caused by carbon formation and/or by the loss of active metal, either by sintering or reaction with the support [3,6]. Under more oxidative conditions such as POM, ATR or SR with a high steam to methane ratio, nickel oxidation and the formation 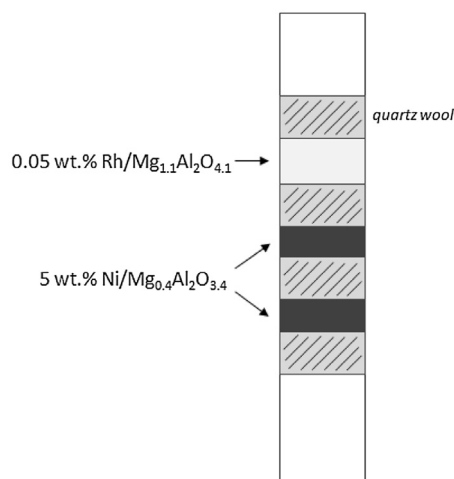of NiAl$_2$O$_4$ have been reported as deactivation causes [4,8–10,24]. The latter reaction conditions are more representative for this study where a mixture of methane, oxygen, water and carbon dioxide was reacted over a nickel-based catalyst. ATR of methane proceeds first by oxidation of the methane by oxygen present in the feed into carbon dioxide and water, taking place at the inlet section of the catalyst bed. This reaction is very exothermic and leads to a localized hot spot in the catalyst bed. The combustion of methane fully consumes the oxygen present in the feed. Due to the oxidative atmosphere in the combustion zone, the nickel is oxidized into nickel oxide, which can catalyze methane combustion. Methane reforming takes place downstream in the reactor
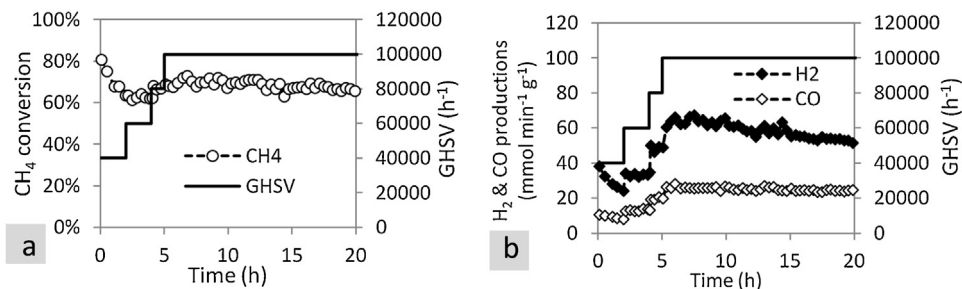

Fig. 14. a) CH$_4$ conversion and b) H$_2$ and CO productions (mmol min^{-1} g^{-1}) during ATR of model biogas on RM1.1. Reaction conditions T = 700 °C, Steam/CH$_4$ = 3, O$_2$/CH$_4$ = 0.5, CO$_2$:CH$_4$ = 40:60, GHSV ranging from 40 000 to 100 000 h^{-1}.
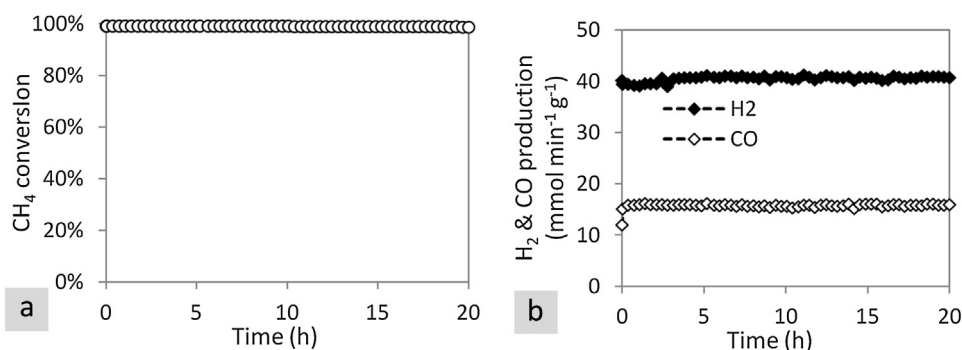
Fig. 16. a) CH_4 conversion and b) H_2 and CO productions (mmol min^{-1} g^{-1}) during ATR of model biogas on dual-catalyst bed composed of 8 mg of RM1.1 and 20 mg of NM0.4. Reaction conditions T = 700 °C, Steam/CH_4 = 3, O_2/CH_4 = 0.5, CO_2:CH_4 = 40:60, GHSV = 57 000 h^{-1}.
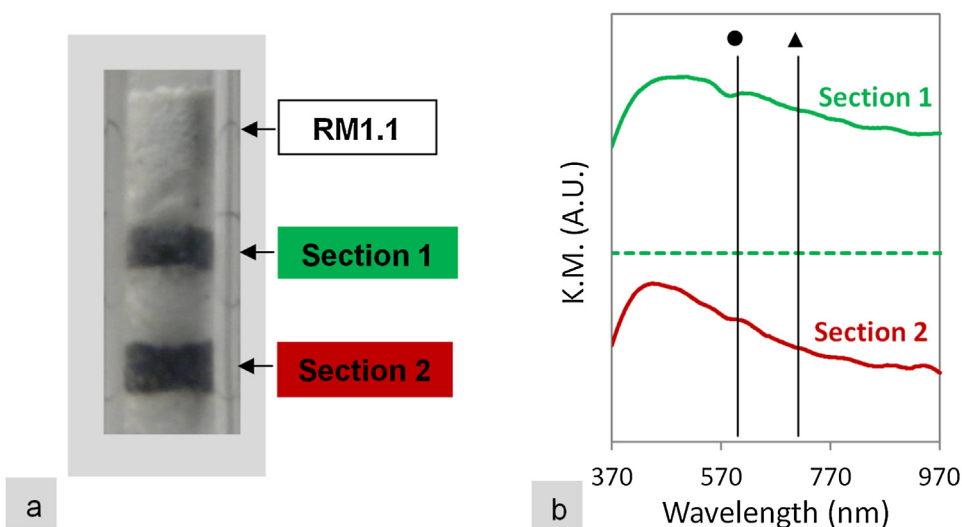

Fig. 17. a) Photograph of the reactor after reaction and b) Kubelka-Munk Spectra of sections 1 and 2 of 5 wt.% Ni/$Mg_{0.4}Al_2O_{3.4}$ after test over dual-bed catalysts (m = 2 × 10 mg).

where all oxygen is depleted, mainly by reaction with steam and to a lesser extend with carbon dioxide. These two reactions are highly endothermic leading to a cold spot in the reactor, as evidenced in Fig. 4b. At the same time and continuing downstream in the catalyst bed, the water gas shift (or reverse) reaction will take place. The reforming and WGS reactions are catalyzed by metallic nickel.

During the ATR of the model biogas mixture over Ni/$MgAl_2O_4$ complete methane conversion is observed over a certain period of time, which depends on the reaction conditions and catalyst composition, followed by a sharp drop of the methane conversion to zero with concurrent drop of the syngas production (Figs. 3 and 12). This deactivation profile is very different from the profiles reported for coking or sintering of the catalysts, where a gradual decrease of the conversion with time is observed. At the same time temperature measurements inside the catalyst bed show that the hot spot moves from the reactor inlet to the outlet during catalyst deactivation. This hot spot is associated with the zone where methane combustion takes place. In contrast to previous studies relating Ni catalysts deactivation to the oxidation of nickel [10,11], the present results shows that the formation of NiO in the combustion zone is not directly responsible for catalyst deactivation, but indirectly through the reaction of NiO with the support and the formation of a Ni spinel phase. It should be mentioned that this spinel phase is not necessarily a pure and stoichiometric phase such as $NiAl_2O_4$ but any sub-stoichiometric possible composition $(MgNi)_{1-x}Al_2O_{4-x}$ (x = 0–1) might be formed. Thus the first process in the overall catalyst deactivation is the loss of the active sites for

methane combustion, by conversion of NiO into inactive spinel in the high temperature zone. $NiAl_2O_4$ is essentially inactive for both methane combustion and methane reforming, as shown in Fig. 5 (no more than 3–6% methane conversion). Once the active sites for methane combustion at the inlet of the catalyst bed are deactivated, the combustion will take place further down the bed, by converting the metallic nickel into NiO. This process will continue until the end of the catalyst bed is reached and all oxidation sites have been deactivated. This is consistent with the fact that the methane conversion drops to zero, while if only methane combustion took place without any reforming reactions, the amount of oxygen in the feed would lead to 25% CH_4 conversion.

NiO reacts with alumina to form inactive $NiAl_2O_4$ [4,8,9], through the diffusion of Ni^{2+} ions into the tetrahedral cationic vacancies present in γ-Al_2O_3. Thus the presence of NiO and high temperatures favor the formation of $NiAl_2O_4$. $MgAl_2O_4$ used here as support in place of Al_2O_3 is expected to prevent or at least limit the diffusion of nickel ions into the vacancies. However, UV–vis-DRS analyses evidenced the presence of some $NiAl_2O_4$ after reaction. This might be related to the different crystal structures of the two spinels, $MgAl_2O_4$ and $NiAl_2O_4$.

$MgAl_2O_4$ has a "normal" spinel structure (space group $Fd3m$) with a unit cell made from a cubic close-packed 32 oxygen atoms sub-lattice, defining 64 tetrahedral and 32 octahedral interstices [17,25]. The full spinel formula is given by $Mg_8Al_{16}O_{32}$. The 8 Mg^{2+} cations occupy exclusively tetrahedral sites, whereas the 16 Al^{3+} cations reside in octahedral sites. Only 1/8 of the tetrahedral sites

and 1/2 of the octahedral sites are occupied by cations, which means that many cationic sites are vacant.

On the other hand, pure $NiAl_2O_4$ is considered to be a partially "inverse" spinel. In purely inverse spinels such as $NiFe_2O_4$, one half of the Fe^{3+} cations occupy tetrahedral sites, whereas the residual Fe^{3+} and all Ni^{2+} cations are both octahedrally coordinated [26]. In most spinel structures, however, cation ordering always accommodates a significant amount of disorder and is generally intermediate between the normal and inverse structures. $NiAl_2O_4$ structure is only partially inverse, since Ni^{2+} cations can occupy both octahedral and tetrahedral sites [25,26]. Despite the fact that Ni^{2+} ions are more stable in octahedral coordination because the high crystal field stabilization energy of Ni^{2+} ions favors this coordination, anomalous X-ray scattering has shown that about 15% of Ni^{2+} cations of $NiAl_2O_4$ occupy tetrahedral sites [26].

The temperature has also a strong influence on disorder and cation inversion in normal and inverse spinels: the degree of disorder increases steadily from about 15% at 800 K up to 35% at 1800 K [27]. Mg^{2+} and Ni^{2+} cations have the same valence and similar effective ionic radii (0.72 and 0.69 Å, respectively, in six-fold coordination [28]), but although Mg^{2+} ions should preferentially occupy tetrahedral sites whereas Ni^{2+} ions should prefer octahedral coordination, the spinel structure appears versatile enough for Ni^{2+} and Mg^{2+} cations to diffuse in both tetrahedral and octahedral sites at the high temperature reached in the methane combustion zone. The combination of high temperatures, disorder in the $MgAl_2O_4$ crystal structure and presence of NiO leads to the formation of an inactive nickel spinel, assumed to be $NiAl_2O_4$, but any sub-stoichiometric possible composition $(MgNi)_{1-x}Al_2O_{4-x}$ (x = 0–1) could also be formed.

The catalyst stability increases with an increasing Mg content (Fig. 12). Adjusting the Mg:Al ratio to 1.1:2 clearly slowed down the diffusion rate of nickel ions into the support. NM0.4 deactivated before NM0.7 and both deactivated before NM1.1. Redfern et al. [27] pointed out that Mg-deficiency significantly reduces the degree of order in the $MgAl_2O_4$ spinel. Therefore, the Mg/Al stoichiometry appears to be a critical parameter. Moreover, the fact that NM0.4 and NM0.7 deactivated more quickly when the GHSV was increased from 40 000 to 60 000 h^{-1} pointed out that the higher the temperature, the quicker the spinel was formed. Indeed, as the GHSV was increased, the quantities of O_2 and CH_4 at the inlet increased as well, leading to a higher hot spot temperature.

The deactivation of the $Ni/MgAl_2O_4$ catalyst as described above was confirmed by UV–vis-DRS analysis and visual inspection of the four catalyst bed sections as a function of time on stream. After reduction at 800 °C, most of the nickel was present as metallic nickel whereas after a short period of time on stream, a part of the inlet section was turned into a mixture of NiO and $NiAl_2O_4$, with the remaining of the bed being metallic nickel. Progressively, from the inlet towards the reactor outlet the metallic nickel turned into $NiAl_2O_4$.

Finally, by using a rhodium-based catalyst to ensure the methane combustion at the reactor inlet, the deactivation of the $Ni/MgAl_2O_4$ reforming catalyst could be prevented. Rhodium is a stable combustion catalyst, and although it is also oxidized in the presence of oxygen, Rh oxides are not stable at high temperature and decompose into metallic Rh, preventing its reaction with the support. All the oxygen present in the feed is converted over the rhodium catalyst. Consequently, the $Ni/MgAl_2O_4$ catalyst is now no longer exposed to molecular oxygen and the nickel remains in the metallic state.

No direct access to the reaction kinetics is possible from the experimental data, as the reaction rates at these temperatures are very high. This is reflected by the complete initial methane conversion for all samples. A first analysis of the mass and heat transfer criteria indeed showed that the rate is limited by external
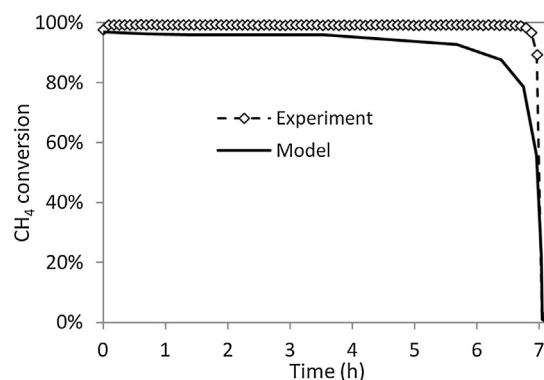

Fig. 18. Comparison between the experimental methane conversion over NM0.4 (presented in Fig. 3) and the simulated conversion.

heat transfer and internal mass transfer. To describe the deactivation mechanism in a more quantitative manner, the methane conversion as a function of time was simulated for fixed bed reactor under steady-state conditions. A one-dimensional plug flow model including an energy balance was used. The model equations correspond to the basic one-dimensional model combined with the equivalent one dimensional model approach as described in [29]. The differential equations were solved numerically using an ODE integrator. The kinetics for the ATR reaction were taken from a study by Schouten et al. [30], which is based on a combination of the oxidation kinetics originally proposed by Trimm and Lam [31] and the well-known reforming kinetics from Xu and Froment [32]. A linear decrease of the number of sites as function of time, progressively from the inlet of the reactor towards the outlet was assumed, as suggested by the equally spaced measured hot spots shown in Fig. 3. The simulation showed a hot spot at the entrance of the catalytic bed in good agreement with the experiment (Fig. 4). By lowering the active sites the hot spot moves down the bed, but the simulation showed that the methane conversion was hardly impacted until most of the active sites were considered as inactive. Fig. 18 shows a comparison between the simulated and experimental methane conversion as a function of time on stream. The model is able to predict the sudden decrease in the methane conversion, which occurs when more than 80% of the sites are deactivated. Under these conditions the rate of deactivation amounted to 6 μmol (sites)/kg$_{cat}$/s.

5. Conclusion

The deactivation process of Ni-based catalysts during ATR of model biogas was identified by monitoring the temperature profile during reaction and by performing UV–vis-DRS analyses on consecutive catalytic bed sections at various reaction times. A methane combustion zone was located at the catalyst bed inlet, creating a hot spot where metallic nickel was readily oxidized as long as molecular oxygen was present. NiO was active for CH_4 combustion, which led to O_2 depletion at the inlet while the unconverted methane was reformed downstream on the remaining metallic Ni sites. However, the high temperature in the combustion zone, especially favored by high space velocities, led to the diffusion of Ni^{2+} ions into $MgAl_2O_4$ spinel structure forming an $NiAl_2O_4$ phase, which was inactive for both methane combustion and reforming. The methane combustion zone was shown to move gradually downstream until complete catalyst deactivation. The methane conversion profiles could be adequately described by a kinetic model that included a linear decrease of the number of Ni active sites with time.

NM1.1 was more resistant to deactivation than NM0.4. Increasing the Mg:Al ratio slowed down the diffusion rate of nickel ions

into the support but did not completely prevent it, since the spinel structure can accommodate Ni cations in both tetrahedral and octahedral coordination sites. A different strategy was implemented by using a dual-bed system composed of a Rh catalyst placed on top of a Ni catalyst, both supported on magnesium spinel. The Rh catalyst ensured the efficient combustion of methane leading to complete O_2 conversion. When the Rh was placed at the bed inlet, no $NiAl_2O_4$ formation was identified after reaction, since the Ni was protected from oxidation at high temperatures. For further investigations, some optimizations could be considered in terms of bed lengths, Rh content and Ni content.

Acknowledgement

References

[1] G. Jones, J. Jakobsen, S. Shim, J. Kleis, M. Andersson, J. Rossmeisl, F. Abildpedersen, T. Bligaard, S. Helveg, B. Hinnemann, J. Catal. 259 (2008) 147.
[2] P. Ferreira-Aparicio, A. Guerrero-Ruiz, I. Rodríguez-Ramos, Appl. Catal. A Gen. 170 (1998) 177.
[3] H.J. Alves, C. Bley Junior, R.R. Niklevicz, E.P. Frigo, M.S. Frigo, C.H. Coimbra-Araújo, Int. J. Hydrogen Energ. 38 (2013) 5215.
[4] J.R. Rostrup-Nielsen, Catalytic steam reforming, Catalysis 5 (1984) 1.
[5] J. Sehested, Catal. Today 111 (2006) 103.
[6] K. Takehira, T. Shishido, P. Wang, T. Kosaka, K. Takaki, J. Catal. 221 (2004) 43.
[7] J. Sehested, A. Carlsson, T.V.W. Janssens, P.L. Hansen, A.K. Datye, J. Catal. 197 (2001) 200.
[8] A.M. Gadalla, B. Bower, Chem. Eng. Sci. 43 (1988) 3049.
[9] D. Dissanayake, M.P. Rosynek, K.C.C. Kharas, J.H. Lunsford, J. Catal. 132 (1991) 117.
[10] S. Araki, N. Hino, T. Mori, S. Hikazudani, Int. J. Hydrogen Energ. 34 (2009) 4727.
[11] K. Nagaoka, A. Jentsyn, J. Lercher, J. Catal. 229 (2005) 185.
[12] S. Ayabe, H. Omoto, T. Utaka, R. Kikuchi, K. Sasaki, Y. Teraoka, K. Eguchi, Appl. Catal. A Gen. 241 (2003) 261.
[13] Z. Mosayebi, M. Rezaei, A.B. Ravandi, N. Hadian, Int. J. Hydrogen Energ. 37 (2012) 1236.
[14] X. Cai, Y. Cai, W. Lin, J. Nat. Gas Chem. 17 (2008) 201.
[15] J.C. Escritori, S.C. Dantas, R.R. Soares, C.E. Hori, Catal. Commun. 10 (2009) 1090.
[16] D.C.R.M. Santos, L. Madeira, F.B. Passos, Catal. Today 149 (2010) 401.
[17] K.E. Sickafus, J.M. Wills, N.W. Grimes, J. Am. Ceram. Soc. 82 (1999) 3279.
[18] M. Luneau, Y. Schuurman, F.C. Meunier, C. Mirodatos, N. Guilhaume, Catal. Sci. Technol. 5 (2015) 4390.
[19] B. Scheffer, J.J. Heijeinga, J.A. Moulijn, J. Phys. Chem. 91 (1987) 4752.
[20] R. López-Fonseca, C. Jiménez-González, B. de Rivas, J.I. Gutiérrez-Ortiz, Appl. Catal. A Gen. 437–438 (2012) 53.
[21] F. Meng, G. Chen, Y. Wang, Y. Liu, Int. J. Hydrogen Energ. 35 (2010) 8182.
[22] G.C.M. Tong, J. Flynn, C.A. Leclerc, Catal. Lett. 102 (2005) 131.
[23] B.N.T. Nguyen, C.A. Leclerc, J. Power Sources 163 (2007) 623.
[24] N. Miletic, U. Izquierdo, I. Obregon, K. Bizkarra, I. Agirrezabal-Telleria, L. Bario, P. Arias, Catal. Sci. Technol. 5 (2015) 1704.
[25] M. Jitianu, A. Jitianu, M. Zaharescu, D. Crisan, R. Marchidan, Vib. Spectrosc. 22 (2000) 75.
[26] K. Shinoda, K. Sugiyama, K. Omote, Y. Waseda, Int. J. Soc. Mater. Eng. Resour. 4 (1996) 20.
[27] S.A.T. Redfern, R.J. Harrison, H.S.C. O'Neill, D.R.R. Wood, Am. Mineral. 84 (1999) 299.
[28] R.D. Shannon, Acta Crystallogr. A 32 (1976) 751.
[29] G.F. Froment, K.B. Bischoff, Chemical Reactor Analysis and Design, 2nd edition, Wiley, 1990.
[30] M. Halabi, M. Decroon, J. Vanderschaaf, P. Cobden, J. Schouten, Chem. Eng. J. 137 (2008) 568.
[31] D.L. Trimm, C.W. Lam, Chem. Eng. Sci. 36 (1980) 1405.
[32] J. Xu, G.F. Froment, AIChE 35 (1989) 88.